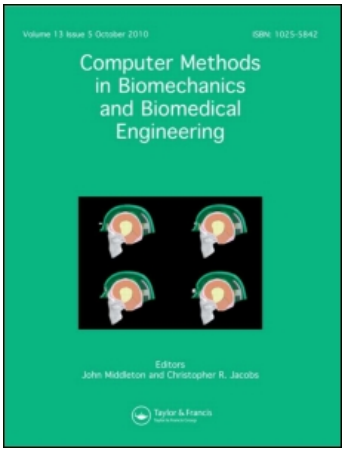

Computer Methods in Biomechanics and Biomedical Engineering
Publication details, including instructions for authors and subscription information:
http://www.informaworld.com/smpp/title~content=t713455284

Evaluation of accuracy of non-linear finite element computations for surgical simulation: study using brain phantom

J. Ma[a]; A. Wittek[a]; S. Singh[a]; G. Joldes[a]; T. Washio[b]; K. Chinzei[b]; K. Miller[a]
[a] Intelligent Systems for Medicine Laboratory, School of Mechanical Engineering, The University of Western Australia, Perth-Crawley, Western Australia, Australia [b] Surgical Assist Technology Group, Institute for Human Science and Biomedical Engineering, National Institute of Advanced Industrial Science and Technology, Ibaraki, Japan

Online publication date: 09 December 2010

To cite this Article Ma, J. , Wittek, A. , Singh, S. , Joldes, G. , Washio, T. , Chinzei, K. and Miller, K.(2010) 'Evaluation of accuracy of non-linear finite element computations for surgical simulation: study using brain phantom', Computer Methods in Biomechanics and Biomedical Engineering, 13: 6, 783 — 794
To link to this Article: DOI: 10.1080/10255841003628995
URL: http://dx.doi.org/10.1080/10255841003628995

Computer Methods in Biomechanics and Biomedical Engineering
Vol. 13, No. 6, December 2010, 783–794

Taylor & Francis
Taylor & Francis Group

Evaluation of accuracy of non-linear finite element computations for surgical simulation: study using brain phantom

J. Ma[a], A. Wittek[a]*, S. Singh[a], G. Joldes[a], T. Washio[b], K. Chinzei[b] and K. Miller[a]

[a]*Intelligent Systems for Medicine Laboratory, School of Mechanical Engineering, The University of Western Australia, 35 Stirling Highway, Perth-Crawley 6009, Western Australia, Australia;* [b]*Surgical Assist Technology Group, Institute for Human Science and Biomedical Engineering, National Institute of Advanced Industrial Science and Technology, AIST Tsukuba East, 1-2-1 Namiki, Tsukuba, Ibaraki 305-8564, Japan*

(*Received 27 June 2009; final version received 15 January 2010*)

In this paper, the accuracy of non-linear finite element computations in application to surgical simulation was evaluated by comparing the experiment and modelling of indentation of the human brain phantom. The evaluation was realised by comparing forces acting on the indenter and the deformation of the brain phantom. The deformation of the brain phantom was measured by tracking 3D motions of X-ray opaque markers, placed within the brain phantom using a custom-built bi-plane X-ray image intensifier system. The model was implemented using the ABAQUS^{TM} finite element solver. Realistic geometry obtained from magnetic resonance images and specific constitutive properties determined through compression tests were used in the model. The model accurately predicted the indentation force–displacement relations and marker displacements. Good agreement between modelling and experimental results verifies the reliability of the finite element modelling techniques used in this study and confirms the predictive power of these techniques in surgical simulation.

Keywords: finite element method; surgical simulation; bi-plane X-ray image intensifier system

1. Introduction

The development of surgical simulation systems requires accurate modelling of soft organs and their interactions with surgical instruments in typical surgical procedures such as needle insertion, incision and dissection. Phenomenological models are by far the most popular approach used in surgical simulation. Such models rely on fitting various functions to experimentally obtained force–displacement curves to simulate the interactions between surgical instruments and soft tissue. For instance, phenomenological models have been utilised to simulate needle insertion into soft tissue in which the needle forces are described as functions of insertion depth and relative velocity between the needle and soft tissue (Simone and Okamura 2002; DiMaio and Salcudean 2003, 2005; Okamura et al. 2004). Application of phenomenological models made it possible to build interactive simulators with real-time kinaesthetic and visual feedback (DiMaio and Salcudean 2005). However, the results predicted by such models are valid only for the specific surgical instruments and boundary conditions of the organs used in the experiments from which the models were derived. This implies that their predictive power is very limited.

Applying appropriate methods of computational solid mechanics to predict the forces acting on surgical instruments and soft tissue deformations during surgery eliminates this drawback. In practice, the finite element method has been used for such predictions; see e.g. Alterovitz et al. (2003), Hing et al. (2007), Wittek et al. (2008) and Jordan et al. (2009). With notable exception of Wittek et al. (2008), previous studies generally used linear finite element procedures for surgical simulation. However, it should be noted that the key assumptions of linear elasticity regarding the infinitesimally small deformations and linear stress–strain relations of soft tissue are violated in a typical surgical procedure. This is because that the surgical procedures typically induce large local deformations and can lead to rigid body motion of the entire organ (Hing et al. 2007; Wittek et al. 2007, 2008). Moreover, it is well documented that soft tissues exhibit non-linear constitutive behaviour (Fung 1993; Mendis et al. 1995; Bilston et al. 1997, 2001; Miller and Chinzei 1997, 2002; Farshad et al. 1999; Miller et al. 2000). Therefore, in surgical simulations, non-linear finite element procedures that take into account both geometric (i.e. finite deformations) and constitutive non-linearities must be used.

Non-linear finite element procedures implemented in the commercial finite element code LS-DYNA^{TM} (Livermore, CA, USA) have been used by Wittek et al. (2008a) to predict the instrumental forces and soft tissue deformations during needle insertion and indentation into the swine brain. The predicted force was approximately

*Corresponding author. Email: adwit@mech.uwa.edu.au

ISSN 1025-5842 print/ISSN 1476-8259 online

DOI: 10.1080/10255841003628995
http://www.informaworld.com

25% larger in indentation and approximately 30% lower in needle insertion than the experimental measurement.

When modelling such complex phenomena as indentation or needle insertion into an actual organ, it is very difficult to distinguish between the inaccuracies due to numerical techniques used (e.g. the reliability of the finite element model degenerates when the elements become severely distorted due to large deformations) and modelling uncertainties regarding the constitutive properties of soft tissue and boundary conditions of an organ. Generic properties are not sufficient for patient-specific computations in surgery simulations because of large variability inherent to biological tissues (Miller 2002; Miller et al. 2010). Despite recent progress in elastography using ultrasound (Salcudean et al. 2006) and magnetic resonance (MR) (McCracken et al. 2005; Sinkus et al. 2005), commonly accepted methods of measuring patient-specific properties of the brain tissue have not been established. Appropriate formulation of boundary conditions for an organ also poses significant challenges (Wittek et al. 2007; Miller et al. 2010). For instance, there are very limited quantitative data about the mechanical properties of the brain meningeal layers and interactions between these layers that can be used to formulate boundary conditions for the brain.

Therefore, in this paper, the reliability and accuracy of non-linear finite element modelling in application to surgical simulation was evaluated through its application in modelling of indentation of the human brain phantom. Replacing the actual brain with the brain phantom allowed us to conduct experiments under accurately controlled conditions and eliminate the uncertainties due to the challenges of formulating appropriate boundary conditions and determining patient-specific constitutive properties for the brain. The evaluation of the finite element model accuracy was conducted in terms of its ability to predict the forces acting on the surgical instrument (indenter) and the deformations due to these forces. Deformation of the brain phantom was determined by tracking 3D motions of the X-ray opaque markers placed within the brain phantom. To facilitate the construction of this marker pattern, the brain phantom was prepared layer-by-layer.

The experiment and modelling techniques were verified on a multiple-layered cylindrical soft tissue phantom that was made using the same material and layer-by-layer manufacturing techniques as the human brain phantom (Ma et al. 2009).

As indicated in the study scheme shown in Figure 1, the subsequent sections of this paper present the following topics: Section 2 describes the experiment set-up and determination of the marker displacements. Section 3 deals with the non-linear finite element modelling of indentation of the brain phantom. Section 4 compares the experimental and modelling results. The discussions and conclusions are presented in Section 5.

2. Experiment

2.1 Preparation of the human brain phantom

The human brain phantom (Figure 2) was made of *Sylgard® 527* A&B silicone gel (Dow Corning Silicones, Midland, MI, USA) which was used by Brands et al. (1999, 2000) to simulate the mechanical responses of brain tissue. X-ray opaque markers (steel beads with a diameter

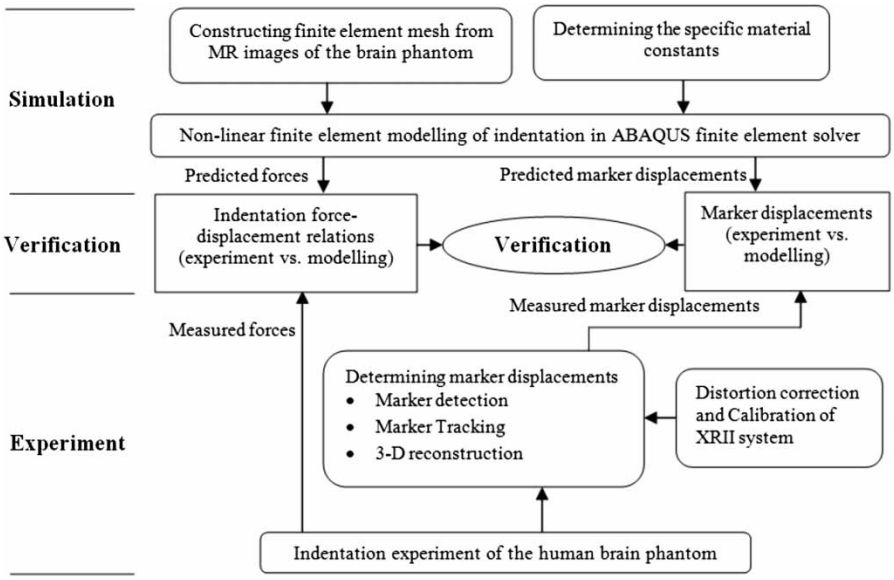

Figure 1. Study scheme.

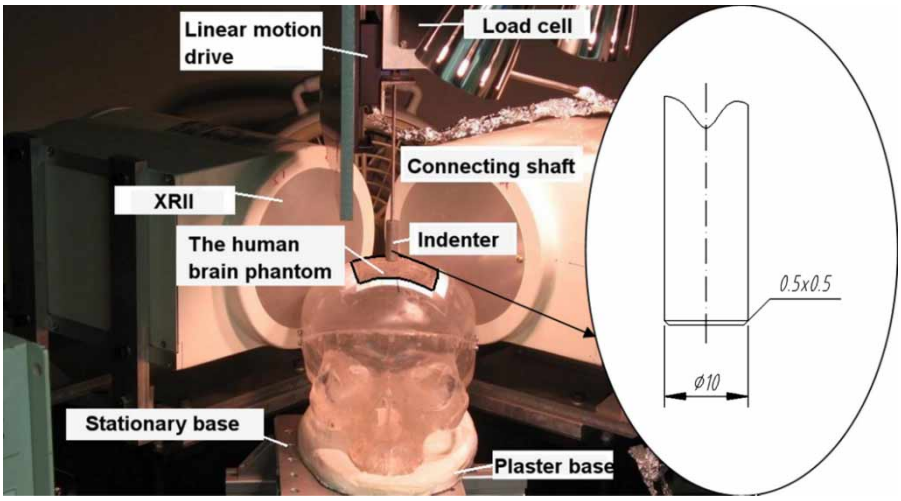

Figure 2. Experiment set-up of brain phantom indentation and indenter geometry. A rectangular hole was opened for the indenter to access the human brain phantom.

of 0.3 mm) were planted within the brain phantom to capture the deformation in the direct neighbourhood of indentation (the part of the brain phantom directly under the indenter). The markers were planted following a pattern designed to minimise occlusion between markers during imaging while sufficiently covering the direct neighbourhood of indentation.

Following the product manual, the *Sylgard® 527* gel was prepared by mixing two parts (*Sylgard® 527* A and B) in the ratio of 1:1. However, as only a small amount of gel was used for each layer, it was difficult to ensure this mixing ratio for every layer. Therefore, it was expected that different gel layers may exhibit different mechanical properties. To facilitate the determination of the specific material constants for each layer, cylindrical samples (height of ~24 mm and diameter of ~30 mm) were made from the batches of gel used in the brain phantom layers. The brain phantom was confined in a human skull cast (3B Scientific, Hamburg, Germany). A rectangular (80 × 40 mm) hole was opened on the top of the human skull cast to allow the indenter to access the brain phantom (Figure 2).

2.2 Experimental apparatus

2.2.1 Experiment set-up

Indentations of the brain phantom were performed using a custom-built apparatus, consisting of a linear motion drive with a load cell and a stationary base as illustrated in Figure 2. The human skull cast that contains the brain phantom was supported by a plaster base glued to the stationary base. The indenter was attached to the load cell by a connecting shaft. Only the forces acting in the longitudinal direction of the indenter were measured and analysed because the indenter was much stiffer than the brain phantom and no indenter or shaft deflection was observed in the experiment.

As illustrated in Figure 2, a solid cylindrical aluminium indenter with a diameter of 10 mm and chamfer of 0.5 × 0.5 mm was used. The indentation speed was kept constant at 1 mm/s and the maximum indentation depth (the indenter displacement was measured from the start of contact between the indenter and the brain phantom until the indenter reached the farthest point of indentation) was approximately 9.5 mm. The displacement of the indenter was measured by a laser range scanner. The indentation forces and indenter displacement were acquired at the sampling rate of 30 Hz.

2.2.2 Bi-plane X-ray image intensifier system for motion tracking

Figure 3 shows the custom-built bi-plane X-ray image intensifier (XRII) system used to track the 3D motions of the X-ray opaque markers planted within the brain phantom. It consists of two sets of X-ray sources and XRII (type E5881J-P1, Toshiba Electron Tubes & Devices, Otawara, Japan) and an imaging acquisition unit (National Instruments, Austin, TX, USA). These two XRIIs were positioned so that their imaging planes were orthogonal to each other, allowing synchronised bi-plane real-time imaging of the marker and indenter motions during indentation experiments. The X-ray images were captured by the image acquisition unit at 30 frames per second and a resolution of 640 × 480 pixels.

When conducting the distortion correction of the X-ray images, the radial and tangential distortions was accounted. The XRII calibration was conducted using a pinhole camera model. Details of distortion correction and calibration are given in the Appendix.

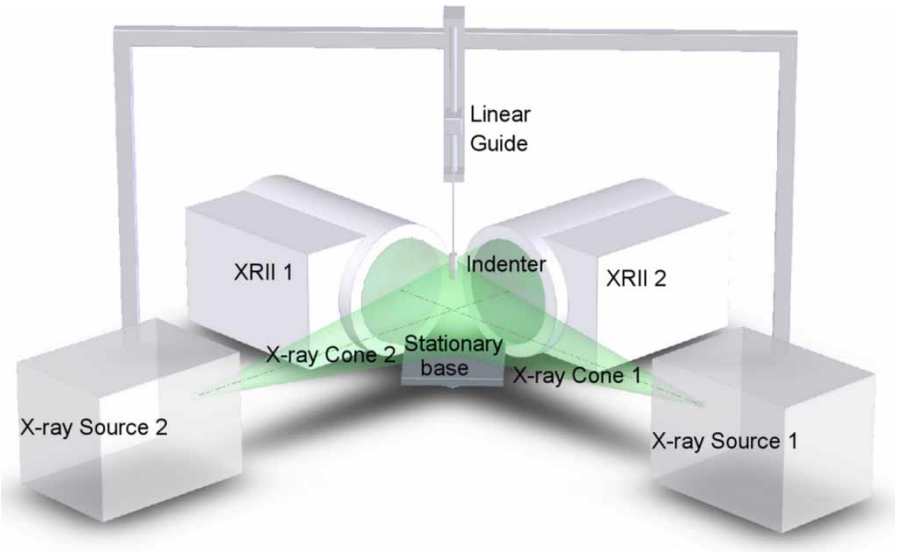

Figure 3. Set-up of the custom-built bi-plane XRII system used to track the 3D motion of the X-ray markers planted in the human brain phantom.

The marker motions were tracked along the X-ray image sequence with an in-house code implemented in Matlab® (The Math Works, Natick, MA, USA). Functions of the Camera Calibration Toolbox for Matlab® (Bouguet c1999–2008) were used to remove the image distortions according to the determined distortion coefficients (for distortion coefficients, see Appendix A). The positions of the markers were extracted from the images using phase congruency corner detection algorithm (Kovesi 2000, 2003, c1996–2007). The tracking code determines the positions of the markers up to a sub-pixel level by fitting a parabola to the neighbourhoods of the markers. To evaluate the accuracy of the results obtained using the tracking code, it was applied to determine the marker positions in 50 image frames in which the markers were kept stationary. The standard deviation of determining the position of a particular marker from these frames was under 0.01 pixels. This is a negligible value comparing with the error due to distortion correction and calibration which was determined to be 2.1 and 1.2 pixels in the left and right views, respectively (for details see Appendix A). Therefore, the accuracy of determining marker positions from X-ray images mainly depends on the accuracy of calibration and distortion correction.

Triangulation functions of the Camera Calibration Toolbox for Matlab® (Bouguet c1999–2008) were used to compute the 3D positions of the markers from their positions in the two perpendicular views determined by the tracking code. From the accuracy of calibration and distortion correction presented in Appendix A, the maximum error in determining the marker positions was determined to be 0.36 mm (3.3 pixels).

2.3 *Determining the specific material constants*

Miller and Chinzei (2002) used the Ogden-type hyperviscoelastic material model to describe the constitutive behaviour of very soft tissue. However, as the *Sylgard® 527* gel used to simulate soft tissue in this study does not exhibit significant strain-rate dependency, the Ogden-type hyperelastic constitutive law (Ogden 1972) was used,

$$W = \frac{2\mu}{\alpha^2}(\lambda_1^\alpha + \lambda_2^\alpha + \lambda_3^\alpha - 3), \tag{1}$$

where W is a potential function, λ_is are principal stretches, μ is the relaxed shear modulus and α is a material coefficient which can assume any value without any restriction. It was noted that a small difference in the mixing ratio of the two parts (*Sylgard® 527* A and B) could result in significant difference in the mechanical properties of the cured gel. Therefore, the cylindrical samples made along with the brain phantom layers were tested by semi-confined uniaxial compression to determine the specific material constants for the layers. In the tests, the top and bottom surfaces of the gel samples were rigidly constrained in the horizontal direction as shown in Figure 4(a) and (b). Consistent with Morriss et al. (2008), the specific material constants of the gel samples were determined by calibrating non-linear finite element models of the compression tests to experimental results. The models were implemented using ABAQUS™ (Providence, RI, USA) finite element solver.

Nine loading cycles were executed on each sample at three different constant loading speeds of 10, 50 and 500 mm/min (0.167, 0.83 and 8.33 mm/s) to assess the repeatability of the results and to evaluate the strain-rate dependency of the gel constitutive properties. The average

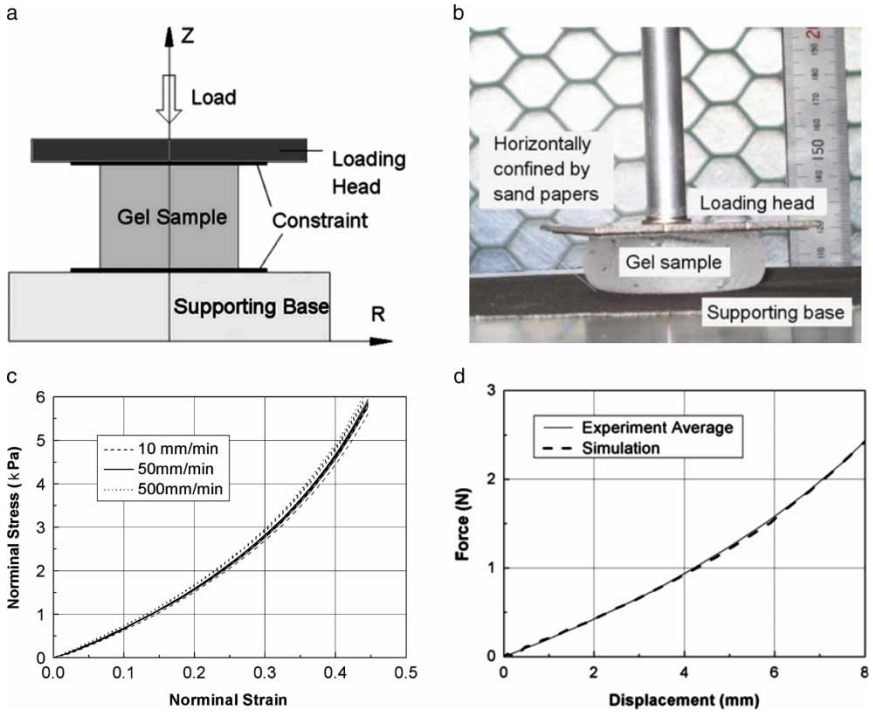

Figure 4. Compression test to determine the material constants. (a) Experiment set-up of the semi-confined uniaxial compression tests. (b) Photograph of compression test. (c) Experimental nominal stress–strain relations at three loading speeds. (d) Comparison of force–displacement relations between experimental average and modelling.

nominal stress–strain relations obtained at three different speeds for one gel sample are shown in Figure 4(c). As clearly indicated in this figure, when the loading speed was increased by 50 times, the relaxed shear modulus increased by less than 5%. Therefore, *Sylgard® 527* gel does not exhibit significant strain-rate dependency. Figure 4(d) shows the typical average force–displacement relations obtained from the experiment and the corresponding modelling results. The Ogden-type hyperelastic material constants (Equation (2.1)) determined for the brain phantom layers are listed in Table 1.

3. Modelling

3.1 Finite element mesh

Anatomically valid organ geometry models are essential for accurate modelling of soft organ deformations in surgical procedures (Hing et al. 2007; Wittek et al. 2007; Miller et al. 2010). The brain phantom geometry was obtained through MR images (Siemens SONATA, 1.5T, Munich, Germany). A digital model of the brain phantom surfaces was constructed from the MR images using 3D Slicer (Available from: http://www.slicer.org) in a Visualisation Toolkit format (Schroeder et al. 2002). Then, this model was converted by an in-house code into a Hypermesh™ (Altair Engineering, Troy, MI, USA)-compatible finite element input file. The Hypermesh™ geometry builder module was used to patch and merge the imported surfaces into a closed surface defining the outer surface of the brain phantom. This surface was used as the boundary when conducting volumetric discretisation using an automatic mesh generator (Hypermesh™) with the second-order tetrahedron elements (type C3D10H in ABAQUS™, 10-node quadratic tetrahedron) (ABAQUS™ Manual, Version 6.7.1). As the *Sylgard® 527* gel used to simulate brain tissue in this study is almost incompressible, second-order elements with mixed formulation and constant pressure were selected to prevent volumetric locking (Belytschko 1983; Joldes et al. 2008). The resulting brain phantom mesh consisted of 41,570 nodes and 27,716 elements (Figure 5).

The characteristic element length of the brain phantom mesh was approximately 5 mm. In order to accurately model the interactions between the indenter and brain phantom, in the indentation area (cylindrical shape of

Table 1. Ogden-type hyperelastic material constants for the layers of the brain phantom determined by calibrating the model of the compression tests to experimental results using ABAQUS™ finite element solver.

Layer	μ (Pa)	α
1	1875	4.9
2	1325	4.1
3	2300	3
4	3000	5

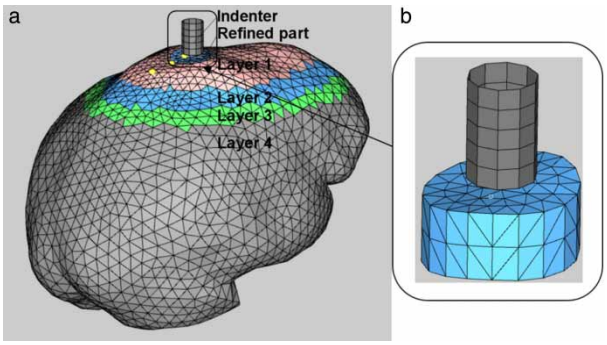

Figure 5. Finite element mesh of the human brain phantom. (a) General view of the mesh, to model the layers structure of the brain phantom, the mesh was divided into element sets according to the layer dimensions. (b) In the indentation area (under the indenter), the mesh was refined to the element characteristic length of 3 mm.

diameter of ~22 mm and height of ~10 mm), the mesh was refined to the characteristic length of 3 mm (Figure 5). To model the multiple-layered structure of the brain phantom, its mesh was divided into four element sets according to the dimensions of the layers (Figure 5).

As the solid cylindrical indenter (diameter of 10 mm with chamfer of 0.5 × 0.5 mm) made of aluminium was in orders of magnitude stiffer than the brain phantom, it was modelled as a rigid body. Therefore, only the surface of the indenter was included in the model to define the contact with the brain phantom. The indenter surface was discretised by 3-node and 4-node shell elements.

3.2 Contact formulations, loading and boundary conditions

When modelling the needle insertion or indentation into soft organ, previous investigators typically applied the loading through prescribed nodal displacements (surgical instruments were not included in the models; Hing et al. 2007; Wittek et al. 2008). Although this is a robust and straightforward approach, the contact interactions between the side of the surgical instrument and the soft tissues are not included. Therefore, to accurately model the interactions between the indenter and the brain phantom, the indentation was modelled as contact interactions between a rigid body (the indenter) and a deformable body (the brain phantom). To account for the direction change of the indenter surface normal, the contact interactions were modelled as two contact pairs: (1) the contact between the head surface of the indenter and the deformable surface of the brain phantom and (2) the contact between the side surface of the indenter and the deformable surface of the brain phantom. For both of the contact pairs, surface-to-surface penalty contact formulations with augmented Lagrange constraint enforcement were applied. When conducting the experiments, it was noted that the *Sylgard® 527* gel stuck firmly to the indenter; therefore, rough friction conditions (no slip is allowed once points are in contact) of ABAQUS™ were used for the contact pairs.

The model was loaded by the motion of the indenter mesh realised by prescribed motion to the reference point. The loading speed was kept constant at 1 mm/s for 9.5 s which corresponded to the maximum indentation depth of 9.5 mm.

The human skull cast that contained the human brain phantom was constrained by the plaster base which was rigidly glued to the stationary base in the experiment (Figure 2). It was noted that the brain phantom stuck firmly to the human skull cast. Therefore, the nodes defining the brain phantom surface except the rectangular hole opened for the indenter to access the brain phantom were rigidly constrained in the model (Figure 6).

4. Results

For Ogden-type hyperelastic material constants (Equation (1)) shown in Table 1, the finite element model accurately predicted the indentation force–displacement relations (Figure 7) and marker displacements (Figures 8–11). For indentation depth up to 9.5 mm, the error in indentation force magnitude is less than 5%. In the experiment, the marker displacements were determined from X-ray images taken by the custom-built bi-plane XRII system. In the simulation, the marker displacements were computed from the nodal displacements predicted by the model

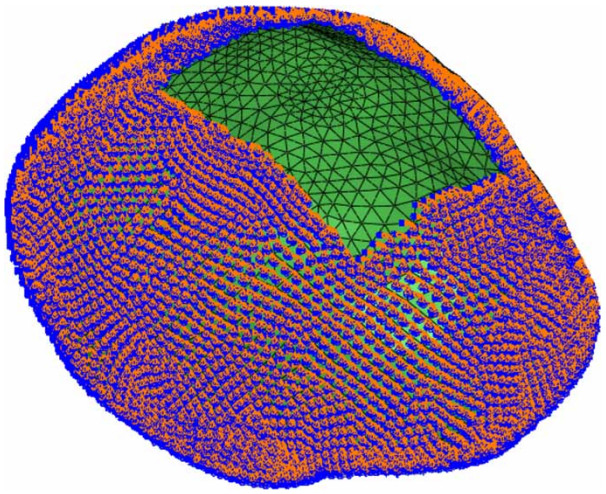

Figure 6. The human skull cast that contains the human brain phantom was confined by the plaster base which was rigidly glued to the stationary base in the experiment. The human brain phantom sticks firmly to the human skull cast. Therefore, the nodes defining the brain phantom surface except the rectangular hole opened for the indenter to access the brain phantom were rigidly confined in the model.

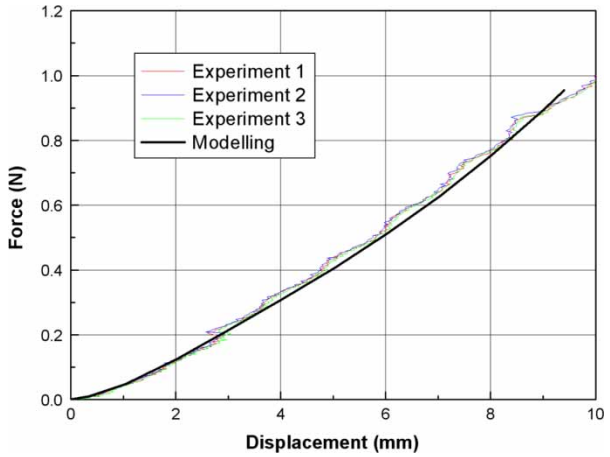

Figure 7. Brain phantom indentation: comparison of modelling and experimental results in force magnitude. The modelling results were obtained with Ogden-type hyperelastic material constants listed in Table 1 using ABAQUS™ finite element solver.

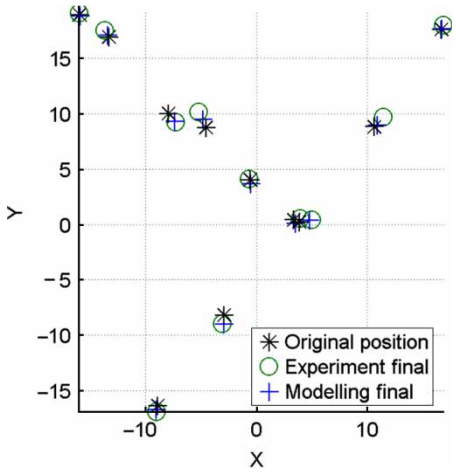

Figure 9. Comparison of the computed and measured final positions of the markers at the indentation depth of 9.5 mm in *XY* plane. Original marker positions are included to indicate the magnitude of displacement.

(interpolation was done using the shape functions of the tetrahedral elements used in the model). Comparison of marker displacement magnitudes at the indentation depth of 9.5 mm between model predictions and experimental measurements is shown in Figure 8. Comparisons of the final positions of the markers in *XY*, *YZ* and *XZ* planes at the same indentation depth are shown in Figures 9–11. Original marker positions are included in this figure to indicate the magnitude of displacements. The maximum, minimum and average differences between the model prediction and experimental measurements in *X*, *Y*, *Z* directions and magnitude of the marker displacements are summarised in Table 2. The average difference of displacement magnitude was 0.32 mm, which is within the accuracy of determining the marker displacements from the X-ray images (see Section 2.2.2). Additional evidence of good agreement between the modelling and experimental deformations is that several markers on the edges of the pattern were found moving upwards in the experimental results and the model accurately predicted this upward motion (Figure 9).

To evaluate the correlation between the experimental and modelling results, a graph was constructed (Figure 12) in which, for every marker, the displacement determined from the experiment is an abscissa and the displacement predicted by the model is an ordinate. The points in Figure 12 closely follow a line oriented at 45° to abscissa and ordinate axes, which indicates very good agreement between the predicted and measured displacements.

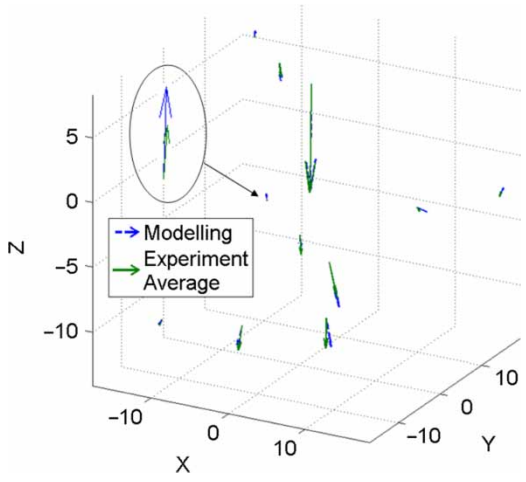

Figure 8. Comparison of the computed and measured marker displacements at the indentation depth of 9.5 mm. The experimental results show that some markers on the edge of the pattern actually moved upwards in the indentation. The model accurately predicted this motion.

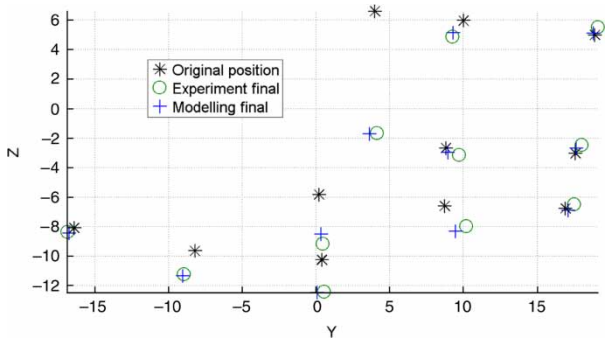

Figure 10. Comparison of the computed and measured final positions of the markers at the indentation depth of 9.5 mm in *YZ* plane. Original marker positions are included to indicate the magnitude of displacement.

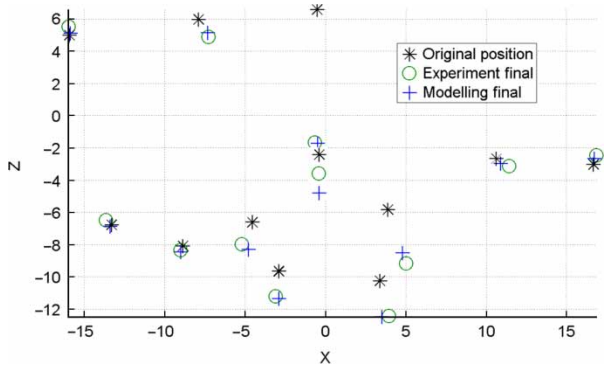

Figure 11. Comparison of the computed and measured final positions of the markers at the indentation depth of 9.5 mm in *XZ* plane. Original marker positions are included to indicate the magnitude of displacement.

Table 2. The maximum, minimum and average differences between the model prediction and experimental measurements in *X*, *Y*, *Z* directions and magnitude of the marker displacements.

Unit: mm	Maximum	Minimum	Average
Displacement in *X* direction	0.52	0.03	0.20
Displacement in *Y* direction	0.72	0.04	0.29
Displacement in *Z* direction	0.64	0.02	0.22
Magnitude	0.83	0.00	0.32

5. Discussion and conclusion

In this paper, the accuracy of non-linear finite element computations in surgical simulation was evaluated through its application in modelling of indentation of the human brain phantom. To distinguish between the inaccuracies due to numerical methods used and inaccuracies due to the modelling uncertainties regarding the boundary conditions of an organ and patient-specific constitutive behaviour of soft tissue, the indentation experiments were conducted on the human brain phantom under accurately controlled conditions. To capture the deformations of the human brain phantom, image processing techniques were used to extract the displacements of the implanted X-ray opaque markers from real-time X-ray images. To account for geometric and material non-linearities, non-linear finite element procedures with implicit time integration methods and Ogden-type hyperelastic material model was used in the model. The brain phantom was made layer-by-layer and the specific material constants of the layers were determined by compressing cylindrical samples made from the batches of gel used in these layers. The indentation was modelled as contact interactions between a rigid body (the indenter) and a deformable body (brain phantom). The finite element model accurately predicted the indentation forces (Figure 7) and marker displacements (Figures 8–11).

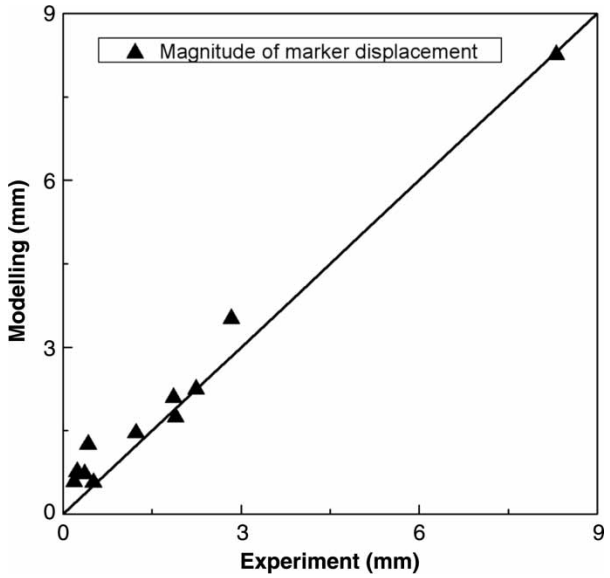

Figure 12. In this figure, the displacement determined from experiment is an abscissa and the displacement predicted by the model is an ordinate. The points closely follow a line oriented at 45° to abscissa and ordinate axes, which indicates very good agreement between the predicted and measured displacements.

It was hypothesised that the minor discrepancies between the modelling and experimental results observed in this study could be attributed to inaccuracies when determining the brain phantom and marker pattern geometry. The brain phantom geometry was obtained through MR images with the resolution of 1 mm. The markers were manually placed using tweezers with reference to a template manufactured with a resolution of 1 mm. Therefore, the accuracy of the brain phantom and marker pattern geometry is not better than 1 mm.

The modelling results demonstrate that for accurately controlled conditions and specific material constants, non-linear finite element models can accurately predict the forces acting on surgical instruments (indenter) and soft organ (simulated by the human brain phantom) deformation due to these forces despite the complexity of the analysed phenomenon related to non-linear constitutive properties, contact interaction between the tool and organ and very large local deformations of the organ. Good agreement between the modelling and experimental results also highlights the predictive power of the non-linear finite element modelling techniques used in this study. With notable exception of Wittek et al. (2008), the previous studies (Simone and Okamura 2002; DiMaio and Salcudean 2003, 2005; Okamura et al. 2004) typically used phenomenological models that rely on fitting various functions to experimentally determined force–displacement relations to determine the forces acting on the surgical instruments. They do not predict but rather describe the soft organ responses. On the other hand, the modelling results presented in this study are results of prediction rather than fitting the model to experiment data. The indentation forces are computed directly from

equations of continuum mechanics. The marker displacements are computed from the nodal displacements predicted by the model. Therefore, the results of this study suggest that, when conducting surgical simulation using non-linear finite element modelling, the main sources of error can be attributed to limited information about boundary conditions for the organs and patient-specific constitutive properties rather than to the limitations of the finite element algorithms.

Acknowledgements

This research has been supported by funds provided by the Australian Research Council (Linkage Grant No. LX0560460) and The University of Western Australia (UWA) 2008 Research Development Award. We would like to thank the Medical Imaging Department of Sir Charles Gardiner Hospital for taking MR images of the human brain phantom and Dr Adrian Keating for making the PVC calibration pattern used in this study.

References

Alterovitz R, Goldberg K, Pouliot J, Taschereau R, I-Chow Hsu. 2003. Needle insertion and radioactive seed implantation in human tissues: simulation and sensitivity analysis. Paper presented at the 2003 IEEE International Conference on Robotics and Automation, Taipei.

Belytschko T. 1983. An overview of semi discretization and time integration procedures. In: Belytschko T, Hughes TJR, editors. Computational methods for transient analysis. Amsterdam: Elsevier. p. 1–65.

Bilston L, Liu Z, Phan-Thien N. 1997. Linear viscoelastic properties of bovine brain tissue in shear. Biorheology. 34(6):377–385.

Bilston L, Liu Z,, Phan-Thien N. 2001. Large strain behaviour of brain tissue in shear: some experimental data and differential constitutive model. Biorheology. 38:335–345.

Bouguet JY. 2009. Documentation of a complete Camera Calibration Toolbox for Matlab [Internet]. c1999–2008. California Institute of Technology; [cited 2009 May 19]. Available from: http://www.vision.caltech.edu/bouguetj/index.html.

Brands DWA, Bovendeerd PH, Peters GW, Wismans JS, Paas MH, van Bree JL. 1999. Comparison of the dynamic behaviour of brain tissue and two model materials. Paper presented at 43rd Stapp Car Crash Conference, Warrendale, PA, USA.

Brands DWA, Bovendeerd PH, Peters GW, Wismans JS. 2000. The large strain dynamic behaviour of *in-vitro* porcine brain tissue and a silicone gel model material. Stapp Car Crash J. 44:249–260.

DiMaio SP, Salcudean SE. 2003. Needle insertion modelling and simulation. IEEE Trans Robot Autom. 19(5):864–875.

DiMaio SP, Salcudean SE. 2005. Needle steering and motion planning in soft tissues. IEEE Trans Biomed Eng. 52(6):1167–1179.

Farshad M, Barbezat M, Flüeler P, Schmidlin F, Graber P, Niederer P. 1999. Material characterization of the pig kidney in relation with the biomechanical analysis of renal trauma. J Biomech. 32(4):417–425.

Fung YC. 1993. Biomechanics: mechanical properties of living tissue. New York, NY: Springer.

Gronenschild E. 1997. The accuracy and reproducibility of a global method to correct for geometric image distortion in the X-ray imaging chain. Med Phys. 24(12):1875–1888.

Gronenschild E. 1999. Correction for geometric image distortion in the X-ray imaging chain: local technique versus global technique. Med Phys. 26(12):2602–2616.

Hartley R, Zisserman A. 2003. Multiple view geometry in computer vision. Cambridge, UK: Cambridge University Press.

Heikkil J, Silven O. 1997. A four-step camera calibration procedure with implicit image correction. Proceedings of the Seventh IEEE Computer Society Conference on Computer Vision and Pattern Recognition: 1106–1113.

Hing JT, Brooks AD, Desai JP. 2007. A biplanar fluoroscopic approach for the measurement, modelling, and simulation of needle and soft-tissue interaction. Med Image Anal. 11(1):62–78.

Joldes G, Wittek A, Miller K. 2008. Non-locking tetrahedral finite element for surgical simulation. Commun Numer Methods Eng. 25(7): 827–836.

Jordan PS, Socrate S, Zickler TE, Howe RD. 2009. Constitutive modelling of porcine liver in indentation using 3D ultrasound imaging. J Mech Behav Biomed Mater. 2(2):192–201.

Kovesi PD. 2000. Phase congruency: a low-level image invariant. Psycho Res. 64(2):136–148.

Kovesi PD. 2003. Phase congruency detects corners and edges. Paper presented at The Australian Pattern Recognition Society Conference. 2003, Sydney.

Kovesi PD. 2009. MATLAB functions for computer vision and image analysis. [Internet]. c1996-2007. The University of Western Australia [cited 2009 May 19]. Available form: http://www.csse.uwa.edu.au/»pk/Research/MatlabFns/.

Ma J, Wittek A, Singh S, Joldes GR, Washio T, Chinzei K, Miller K. 2009. Accuracy of non-linear FE modelling for surgical simulation: study using the soft tissue phantom. Paper presented at Computational Biomechanics for Medicine IV workshop, Medical Image Computing and Computer-Assisted Interventation (MICCAI) 2009, London.

McCracken J, Manduca A, Felmlee J, Ehman RL. 2005. Mechanical transient-based magnetic resonance elastography. Magnet Reson Med. 53(3):628–639.

Mendis K, Stalnaker RL, Advani SH. 1995. A constitutive relationship for large deformation finite element modelling of brain tissue. J Biomech Eng. 117:279–285.

Miller K, Chinzei K. 1997. Constitutive modelling of brain tissue: experiment and theory. J Biomech. 30(11/12):1115–1121.

Miller K, Chinzei K. 2002. Mechanical properties of brain tissue in extension. J Biomech. 35(4):483–490.

Miller K, Chinzei K, Orssengo G, Bednarz P. 2000. Mechanical properties of brain tissue *in-vivo*: experiment and computer simulation. J Biomech. 33(11):1369–1376.

Miller K, Wittek A, Joldes G, Horton A, Dutta Roy T, Berger J, Morriss L. 2010. Modelling brain deformations for computer-integrated neurosurgery. Int J Numer Meth Biomed Engng. 26:117–138.

Mitschke M, Navab N. 2003. Recovering the X-ray projection geometry for three dimensional tomographic reconstruction with additional sensors: attached camera versus external navigation system. Med Ima Anal. 7(1):65–78.

Morriss L, Wittek A, Miller K. 2008. Compression testing of very soft biological tissues using semi-confined configuration – a word of caution. J Biomech. 41(1):235–238.

Navab N, Bani-Hashemi A, Nadar MS, Wiesent K, Durlak P, Brunner T, Barth K, Graumann R. 1998. 3D reconstruction from matrices in a C-arm based 3D-angiography system.

The Proceedings of Medical Image Computing and Computer-Assisted Interventation- MICCAI. 1496: 119–129.

Ogden RW. 1972. Large deformation isotropic elasticity – on the correlation of theory and experiment for incompressible rubberlike solids. Proc R Soc London Ser A, Math Phys Sci. 326(1567):565–584.

Okamura AM, Simone C, O'Leary MD. 2004. Force modelling for needle insertion into soft tissue. IEEE Trans Biomed Eng. 51:1707–1716.

Salcudean S, Turgay E, Rohling R. 2006. Identifying the mechanical properties of tissue by ultrasound strain imaging. Ultrasound Med Bio. 32(2):21–35.

Schroeder W, Martin K, Lorensen B. 2002. The visualization toolkit: an object-oriented approach to 3D graphics. New York, NY: Kitware, Inc.

Simone C, Okamura AM. 2002. Modelling of needle insertion forces for robot-assisted percutaneous therapy. Paper presented at the 2002 IEEE International Conference on Robotics and Automation, Washington DC, USA.

Sinkus R, Tanter M, Xydeas T, Catheline S, Bercoff J, Fink M. 2005. Viscoelastic shear properties of *in vivo* breast lesions measured by MR elastography. Magnet Reson Imaging. 23:159–165.

Weng J, Cohen P, Herniou M. 1992. Camera calibration with distortion models and accuracy evaluation. IEEE Trans Pattern Anal Mach Intell. 14(10):965–980.

Wittek A, Miller K, Kikinis R, Warfield S. 2007. Patient-specific model of brain deformation: application to medical image registration. J Biomech. 40(4):919–929.

Wittek A, Dutta-Roy T, Taylor Z, Horton A, Washio T, Chinzei K, Miller K. 2008. Subject-specific non-linear biomechanical model of needle insertion into the brain. Comput Methods Biomech and Biomed Eng. 11(2):135–146.

Zhang Z. 1999. Flexible camera calibration by viewing a plane from unknown orientations. Paper presented at 1999 International Conference on Computer Vision. Corfu, Greece.

Zhang Z. 2000. A flexible new technique for camera calibration. IEEE Trans Pattern Anal Mach Intell. 22(11):1330–1334.

Appendix A. Distortion correction and calibration

To obtain accurate positions of the markers in the recorded X-ray images, the geometrical distortions of the image need to be removed. In an XRII, there are two main types of distortions: pincushion distortion (positive radial distortion) caused by projecting a flat surface onto a global surface (the input sulphur screen of the XRII) and spiral distortion caused by the deflection of electrons due to earth's magnetic field (Gronenschild 1997, 1999). The CCD camera applied to capture the intensified light image also induces radial distortion and tangential distortion due to imperfection of the lens elements (Weng et al. 1992; Heikkil and Silven 1997; Hartley and Zisserman 2003). In the experiments, the effect of spiral distortion was found to be negligible. Therefore, only radial and tangential distortions were considered. By combining the distortion components, the total distortion $[\delta_x, \delta_y]^T$ at an image point $Q(x,y)$ in the camera reference frame (CRF) can be summarised in the following expression (Weng et al. 1992; Heikkil and Silven 1997; Hartley and Zisserman 2003),

$$\begin{bmatrix}\delta_x\\ \delta_y\end{bmatrix} = \begin{pmatrix}k_1 x r^2 + k_2 x r^4\\ k_1 y r^2 + k_2 y r^4\end{pmatrix} + \begin{bmatrix}2t_1 xy + t_2(r^2 + 2x^2)\\ t_1(r^2 + 2y^2) + 2t_2 xy\end{bmatrix}, \quad \text{(A1)}$$

where (u',v') is the coordinate of point Q with respect to the principal point (centroid) of the image plane; $r = \sqrt{u'2 + v'2}$ is the distance from the point Q to the principal point, k_1, k_2 are the coefficients of radial distortion and t_1, t_2 are the coefficients of tangential distortion.

To reconstruct 3D displacements of the implanted markers, the camera parameters need to be determined through calibration. Following Navab et al. (1998), Mischke et al. (2003), and Hing et al. (2007), the projection geometry of an XRII was approximated by a pinhole camera model illustrated in Figure A1. It can be described as a transformation from the 2D-homogeneous coordinates $u = [u, v, 1]^T$ in the image reference frame (IRF) to 3D-homogeneous coordinates $X = [X, Y, Z, 1]^T$ in the world reference frame (WRF),

$$u = \mathbf{P} \cdot X, \quad \text{(A2)}$$

where $\mathbf{P}$ is the projection matrix that contains the camera parameters. These parameters can be divided into two sets: (1) The intrinsic parameters $\mathbf{A}$ described by the 3×4 matrix define the transformation between IRF and CRF; and (2) the extrinsic parameters $\mathbf{T}$ described by 4×4 homogeneous transformation matrix define the position (t) and orientation (R) of CRF in the WRF (Zhang and Xu 1996; Heikkil and Silven 1997; Hartley and

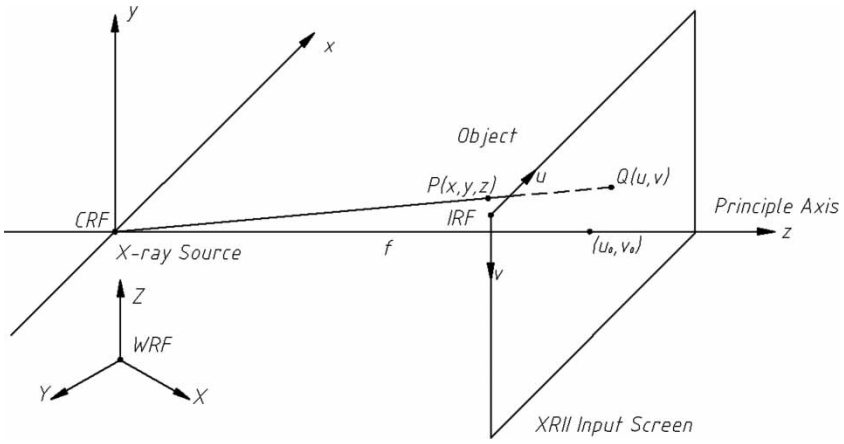

Figure A1. The projection geometry of a distortion-free XRII can be approximated as a pinhole camera model.

Table A1. The estimated distortion coefficients and camera parameters obtained from distortion correction and calibration.

	Distortion coefficients				Camera parameters (pixel)			
XRII parameters	k_1	k_2	t_1	t_2	α_u	α_v	u_0	v_0
Left	3.05	−245.47	−0.019	−0.066	4288.2	4284.6	239.5	319.5
Right	3.00	−194.69	−0.040	0.071	4544.5	4471.9	246.5	313.5

Table A2. The average, maximum and standard deviation of reprojection error indicates the accuracy of determining the 3D position of an object point from the X-ray images.

	In pixel			In millimetres		
Reprojection error	Average error	Standard deviation	Maximum error	Average error	Standard deviation	Maximum error
Left	0.7	0.3	2.1	0.08	0.04	0.23
Right	0.3	0.2	1.2	0.03	0.02	0.13

Zisserman 2003). Using the intrinsic and extrinsic parameters, the camera projection matrix can be expressed as,

$$\mathbf{P} = \mathbf{A} \cdot \mathbf{T} = \begin{bmatrix} \alpha_u & 0 & u_0 & 0 \\ 0 & \alpha_v & v_0 & 0 \\ 0 & 0 & 1 & 0 \end{bmatrix} \cdot \begin{bmatrix} R & t \\ 0^{\mathrm{T}} & 1 \end{bmatrix}, \qquad \text{(A3)}$$

where $(\alpha_u, \alpha_v)^{\mathrm{T}}$ represents the equivalent focal length in terms of pixel dimensions in u and v direction respectively, $(u_0, v_0)^{\mathrm{T}}$ is the coordinate of the principal point of the image plane in pixels.

The camera calibration method proposed by Zhang (1999, 2000) was used to determine the camera parameters and distortion coefficients. The camera parameters and distortion coefficients were computed using the Camera Calibration Toolbox for Matlab® developed by Bouguet (c1999–2008) in which radial and tangential distortions are modelled. The estimated camera parameters and distortion coefficients are listed in Table A1. The average, maximum and standard deviation of reprojection error indicating the accuracy of determining the 3D position of an object point from the X-ray images are provided in Table A2.